BNL-225186-2024-JAAM

Revitalizing Iron Redox by Anion-Insertion-Assisted Ferro- and Ferri-Hydroxides Conversion at Low Alkalinity

F. Guo, A. Abeykoon

To be published in "Journal of the American Chemical Society"

July 2022

Photon Sciences

Brookhaven National Laboratory

U.S. Department of Energy

USDOE Office of Science (SC), Basic Energy Sciences (BES). Scientific User Facilities (SUF)

DISCLAIMER

Revitalizing Iron Redox by Anion-Insertion-Assisted Ferro- and Ferri-Hydroxides Conversion at Low Alkalinity

Fenghua Guo,[a] Sathya Narayanan Jagadeesan,[a] Ranga Teja Pidathala,[b] SaeWon Kim,[a] Xiaoqiang Shan,[a] N Aaron Deskins,[c] AM Milinda Abeykoon,[d] Gihan Kwon,[d] Daniel Olds,[d] Badri Narayanan,* [b] Xiaowei Teng* [a]

[a]Department of Chemical Engineering, University of New Hampshire, Durham, New Hampshire 03824, United States

[b]Department of Mechanical Engineering, University of Louisville, Louisville, Kentucky 40292, United States

[c]Department of Chemical Engineering, Worcester Polytechnic Institute, Worcester, Massachusetts 01609, United States

[d]National Synchrotron Light Source II, Brookhaven National Laboratory, Upton, New York 11973, United States

ABSTRACT

Iron hydroxides are desirable alkaline battery electrodes for low cost and environmental beneficence. However, hydrogen evolution on charging and Fe_3O_4 formation on discharging cause low storage capacity and poor cycling life. We report that green rust (GR) ($Fe^{2+}_4Fe^{3+}_2(HO^-)_{12}SO_4$), formed via sulfate insertion, promotes $Fe(OH)_2$/FeOOH conversion and shows a discharge capacity of ~ 211 mAh g^{-1} in half-cells and coulombic efficiency of 93% after 300 cycles in full-cells. Theoretical calculations show that $Fe(OH)_2$/FeOOH conversion is facilitated by intercalated sulfate anions. Classical molecular dynamics simulations reveal that electrolyte alkalinity strongly impacts the energetics of sulfate solvation, and low alkalinity ensures fast transport of sulfate ions. Anion-insertion-assisted $Fe(OH)_2$/FeOOH conversion, also achieved with Cl^- ion, paves a pathway towards efficient utilization of Fe-based electrodes for sustainable applications.

Developing grid-scale battery systems is essential to store electrical energy generated from intermittent renewable sources.[1] Aqueous batteries using earth-abundant materials and charge carriers beyond Li-ions are low-cost and safe alternatives to their non-aqueous counterparts for grid storage.[2] As the fourth most abundant element in the earth's crust, iron (Fe) potentially satisfies nearly all criteria for a green battery, such as various oxidation states, geographic accessibility, low cost, and environmental benefits.[3] Iron has acted as an anode material in Ni/Fe alkaline batteries[4,5] but faces challenges in modern energy supply systems due to low charging efficiency and poor discharge capability.[6] The discharge (oxidation) of iron anode proceeds primarily to $Fe(OH)_2$ (Eq. 1) and continuous oxidation of $Fe(OH)_2$ hardly forms $Fe(OH)_3$ (Eq. 2) but forms Fe_3O_4 (Eq. 3, **Figure S1**) which impedes the redox process and causes cyclability loss.[7,8] When an iron anode is charged, reducing $Fe(OH)_2$ to Fe is inevitably accompanied by parasitic hydrogen evolution reaction (HER) (**Figure S1**a)[9–11] (Eqs. 1 and 4) with decreased charging efficiency (**Figure S2**).[12] Employing $Fe(OH)_2$/FeOOH redox could avoid the HER and improve the charging efficiency while mitigating Fe_3O_4 formation on discharging has not been reported with spectroscopic evidence. This work focuses on unlocking $Fe(OH)_2$/FeOOH conversion with anion-insertion. When paired with a cocktail electrolyte containing 0.01 M NaOH and 0.2 M Na_2SO_4, $Fe(OH)_2$ first formed a Green Rust (GR) phase on discharging (**Figure S1**b) via intercalation of SO_4^{2-} into $Fe(OH)_2$, and finally formed FeOOH. Density functional theory (DFT) calculations and classical molecular dynamics (CMD) simulations suggested that sulfate and low-alkalinity electrolytes play

essential roles in $Fe(OH)_2$/FeOOH conversion, where sulfates in low alkalinity electrolytes diffuse faster than in high-alkalinity electrolytes and the GR phase with sulfate residing in the interlayer of [FeO_6] frameworks promoted FeOOH formation.

$Fe(OH)_2 + 2e^- \rightarrow Fe + 2OH^-$ $E^0 = -1.017V$ Eq.1

$Fe(OH)_3 + e^- \rightarrow Fe(OH)_2 + OH^-$ $E^0 = -0.700V$ Eq.2

$Fe_3O_4 + 4H_2O + 2e^- \rightarrow 3Fe(0H)_2 + 2OH^-$ $E^0 = -1.164V$ Eq.3

$2H_2O + 2e^- \rightarrow H_2 + 2OH^-$ $E^0 = -0.968V$ Eq.4

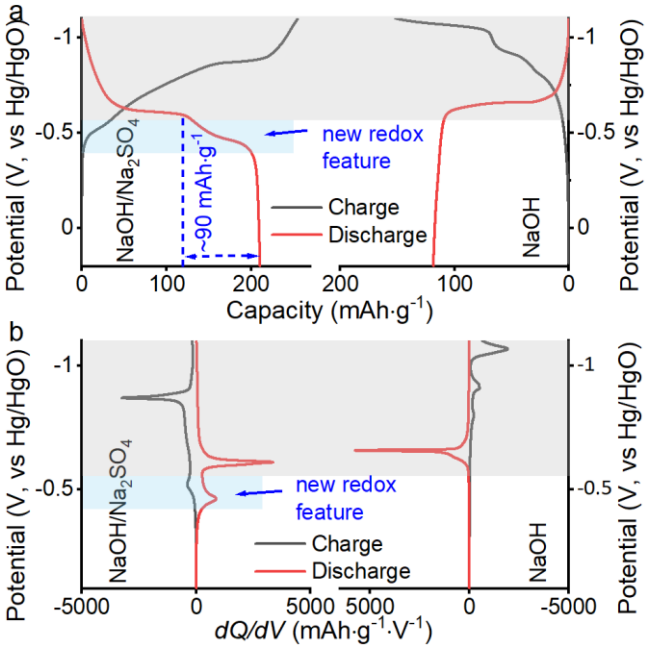

Figure 1. (a) CP and (b) their corresponding dQ/dV curve of FeOOH at a current density of 0.2 A g-1 conducted in a three-electrode half-cell using a 0.01M NaOH solution with and without 0.2 M Na_2SO_4 additive.

FeOOH (JCPDS No.44-1415) particulates were synthesized by reacting ferrous chloride with an ammonium hydroxide solution (**Figure S3**).[13] **Figure 1** showed chronopotentiometry (CP) and dQ/dV plot of FeOOH in a three-electrode half-cell using a 0.01M NaOH solution, with and without 0.2 M Na_2SO_4 additive. The FeOOH showed a higher discharge capacity (211 mAh g^{-1}) in the cocktail electrolytes than in the NaOH electrolyte (119 mAh g^{-1}). The capacity contribution of conducting carbon was measured and can be neglected (**Figure S4**). During discharging, one

plateau (~ 0.60 V) appears in both electrolytes and a new plateau emerged at -0.46 V only in the cocktail electrolytes, accounting for the net discharge capacity of ~ 90 mAh g^{-1}. Similar redox behaviors were observed in cyclic voltammetry (CV) measurements (**Figure S5**).

Figure 2a shows *in situ* XRD patterns in cocktail electrolytes, the unfolded CV curves, and phase analysis from the Rietveld refinement (see waterfall XRD patterns and detailed peak assignment in **Figure S6**a-d).[14,15] Results show that FeOOH was reduced entirely into brucite-type $Fe(OH)_2$ (JCPDS 13-0089) at -1.2 V.[16] As potential increased to -0.48 V, nearly 40% $Fe(OH)_2$ formed Fe_3O_4 (JCPDS 19-0629) (Eq. 3 in reverse). As the potential continued to increase, new peaks appeared at 2θ degrees of 0.86°, 1.73°, and 2.61°, attributing to basal planes with a correlation d(00l) = 11.06Å/l (l = 1, 2, 3) of GR materials $[Fe^{2+}_4Fe^{3+}_2(HO^-)_{12}]^{2+}[(SO_4^{2-})\cdot 6H_2O]^{2-}$ (**Supplementary Table 1**),[17–19] from intercalating SO_4^{2-} into interlayers of $Fe(OH)_2$ (Eq. 5) . As the potential continuously increased to -0.35 V, $Fe(OH)_2$ diminished, and the GR phase reached a maximum molar ratio of 41% (based on Fe atoms). When the potential increased continuously, another new set of peaks appeared at 2θ degrees of 3.73°, 4.24°, and 5.61°, assigned to (1 0 0), (1 0 ±1), and (1 0±2) reflections of δ-FeOOH (JCPDS 13-87).[20] The FeOOH forms at the expense of the GR, suggesting that the removal of SO_4^{2-} from interlayers and protons from $[FeO_6]$ octahedra accounts for the conversion from GR to FeOOH phases (Eq. 6). Notably, the maximum molar fractions of GR and FeOOH are ~ 41 % and ~ 19%, respectively, suggesting that nearly 46% of the GR was converted into FeOOH. Simultaneously, the rest of the GR (54%) formed Fe_3O_4 (Eq. 7). In contrast, $Fe(OH)_2$ formed Fe_3O_4 in NaOH electrolyte (**Figure 2**b, Eq. 1) and there is no evidence of FeOOH formation (**Figure S6**e). Notably, X-ray photoelectron spectroscopy (XPS) measurements (**Figure S7**) show that discharged electrode has a higher Fe^{3+}/Fe^{2+} ratio in cocktail electrolyte than NaOH electrolyte (2.38 vs. 2.08). It suggests a FeOOH molar fraction of 27.5%, close to the value obtained from XRD phase analysis (19%).

$$6Fe(OH)_2 + SO_4^{2-} \rightarrow Fe^{2+}_4Fe^{3+}_2(OH^-)_{12}SO_4 + 2e^- \quad \text{Eq. 5}$$

$$Fe^{2+}_4Fe^{3+}_2(OH^-)_{12}SO_4 + 6OH^- \rightarrow 6FeOOH + SO_4^{2-} + 6H_2O + 4e^- \quad \text{Eq.6}$$

$$Fe^{2+}_4Fe^{3+}_2(OH^-)_{12}SO_4 + 4OH^- \rightarrow 2Fe_3O_4 + SO_4^{2-} + 4H_2O + 2e^- \quad \text{Eq.7}$$

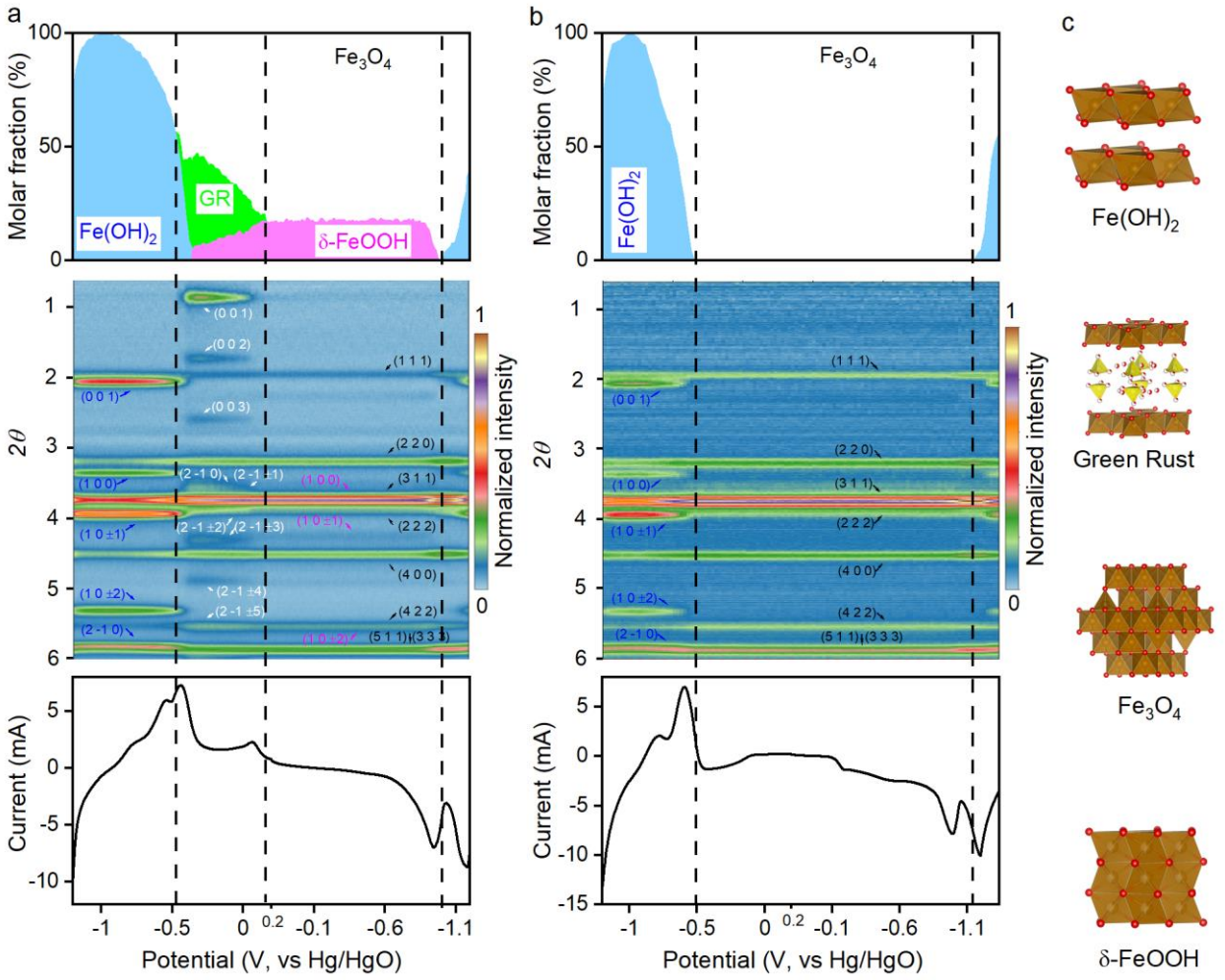

Figure 2. *In situ* XRD of FeOOH in NaOH electrolyte (a) with and (b) without Na_2SO_4 and (c) atomic structures of identified phases.

GR-assisted $Fe(OH)_2$/FeOOH conversion showed superior discharge capacity (211 mAh g^{-1} in the 1st cycle) and capacity retention (93.4%) (**Figure 3**). $Fe(OH)_2/Fe_3O_4$ redox at -0.60 V deteriorated rapidly, while capacities from $Fe(OH)_2$/GR/FeOOH pathway at -0.48V even increased upon cycling. The excellent stability of GR-assisted $Fe(OH)_2$/FeOOH conversion is also manifested in long-term cycling in asymmetric full-cells, showing capacities of 68 mAh g^{-1} and 63 mAh g^{-1} at the 1st and 300th cycles in the NaOH/Na_2SO_4 electrolytes at a current density of 0.2 A g^{-1} with an average coulombic efficiencies of 93% and good rate capabilities (**Figures S8-S11**).

FeOOH→$Fe(OH)_2$ charging process proceeded from 0.2 V to -1.1 V in half-cells and wasn't accompanied by HER. However, when a more negative voltage was applied (-1.2V), the *in*

situ XRD showed the formation of a metallic Fe phase, along with significant HER activities (**Figure S12**). These results suggest metallic Fe might be catalytically more active towards HER than $Fe(OH)_2$, confirmed by DFT calculations (**Figure S13**). Similarly, no HER was observed in the full-cell measurements when the measurements were conducted under a voltage window between 0.1 V and 1.5 V. However, when the upper voltage limit increased from 1.5 V to 1.6 and 1.7 V, HER contribution to the overall charge transfer significantly increased, causing decreased coulombic efficiency and deteriorated capacity retention (**Figure S14**). Notably, full cells using $NaOH/Na_2SO_4$ cocktail electrolytes appear to be more resistant to HER than the NaOH electrolyte, possibly due to the decreased water activity upon the addition of Na_2SO_4 salt.

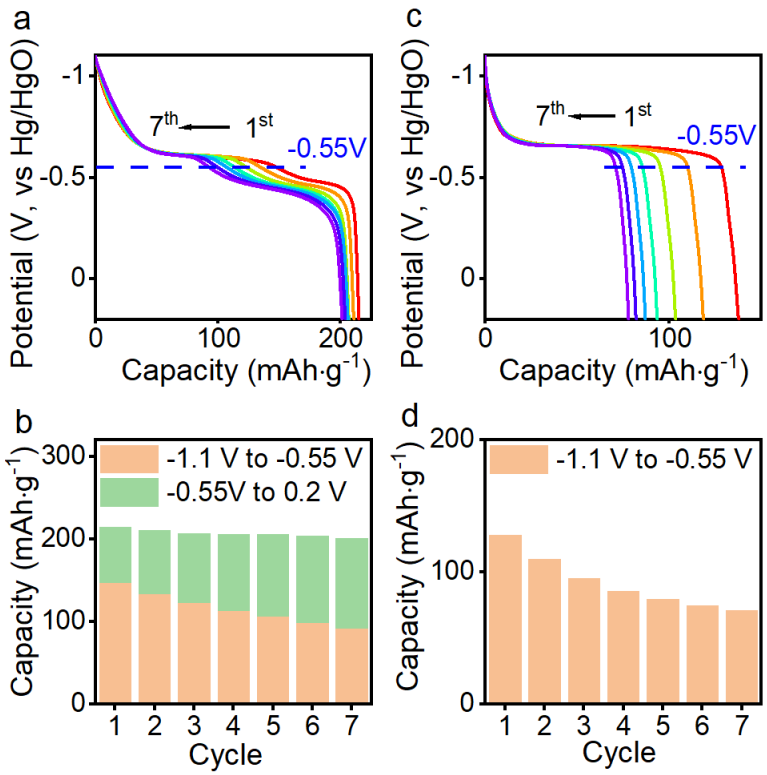

Figure 3. The first seven discharge curves and distribution of capacity of FeOOH in (a, b) 0.01 M NaOH/0.2 M Na_2SO_4 and (c,d) 0.01M NaOH at 0.2 A g^{-1}.

The electrolyte alkalinity plays a critical role in $Fe(OH)_2$/FeOOH conversion (**Figure S15**). CVs show $Fe(OH)_2$/GR/FeOOH features at 0.01 M NaOH with various Na_2SO_4 concentrations but becomes negligible in 0.1M NaOH. This result suggests that high alkalinity solutions favor Fe_3O_4 formation.[21–23] CMD simulations provide atomic-scale insights into the role of electrolyte

alkalinity on the SO_4^{2-} transport through structural water. **Figures 4**a-c show the atomic coordination number around SO_4^{2-}, *Z(r)*, as a function of separation distance, r, by integrating the radial distribution functions over the last 1 ns of CMD trajectories equilibrated under ambient conditions. Similar to previous reports in neutral water,[24–26] we found that sulfates prefer to coordinate with 12 water molecules in the first solvation shell, wherein the closest pairs of sulfur (of sulfate) and oxygen (of water) atoms are within 4.55 Å of each other (**Figure S16**). The atomic coordination in the first solvation shell in 0.01 M NaOH remains nearly identical to that found in neutral water (**Figure 4**a, **S16**). Upon further addition of NaOH, a few OH^- anions begin to appear in the first solvation shell, averaging ~0.11 and ~0.33 OH^- neighbors at 1 M and 2 M NaOH, respectively (**Figure 4**b, c). More importantly, the average number of Na^+ ions in the first solvation shell progressively increases from ~0.5 in 0.01 M NaOH to ~2 in 2 M NaOH (**Figure 4**a-c**, S17**). The increasing presence of Na^+ near SO_4^{2-} enhances thermodynamic stability of solvation clusters at the high alkalinity, as indicated by increasing interaction energy between sulfate and the molecules present in the solvation shell (0.01 M: -166.23 kcal/mol; 2 M: -282.82 kcal/mol) (**Figure 4**d). To explore how the energetics of the solvation cluster affect its lifetime, we analyzed the dynamics of electrostatic/*van der Waals* connectivity between sulfates and water molecules in the solvation shell using the bond correlation function, $C_{S\text{-}W}(t)$ (Details in **Materials and Methods** in SI), similar to established hydrogen bond analysis in aqueous systems.[27] The lifetime of sulfate-water connectivity, τ, is defined such that $C_{(S\text{-}W)}(\tau)=1/e$.[28] **Figure 4**e shows that the lifetime of sulfate-water connectivity within a solvation shell is directly correlated with the stability of the solvation cluster, with an appreciably higher lifetime observed at high NaOH concentrations that feature more stable solvation clusters (2 M: $\tau \sim 24.4$ ps; 0.01 M: $\tau \sim 15.2$ ps). The higher lifetime of SO_4^{2-}-water connectivity under high-alkalinity conditions impedes solvation-desolvation events critical for sulfate transport through the structural water. Indeed, **Figure 4**f shows that sulfate diffusivity through the water in 2 M NaOH is nearly half the value observed in 0.01 M NaOH. Similarly, we also found that the lifetime of hydrogen bonds in water decreases with increasing OH^- concentrations (**Figure S18**), yielding much slower water transport at high alkalinity (2 M NaOH: 1.75×10^{-5} cm^2 s^{-1}; 0.01 M NaOH: 2.83×10^{-5} cm^2 s^{-1}). Such immobilization of water and sulfate in highly alkaline conditions would severely inhibit the kinetics of sulfate-assisted $Fe(OH)_2$/FeOOH conversion (Eq. 6) and consequently promote direct $Fe(OH)_2$/Fe_3O_4 conversion.

This finding is consistent with X-ray experiments, suggesting that low-alkalinity is necessary to drive $Fe(OH)_2$/GR/FeOOH redox.

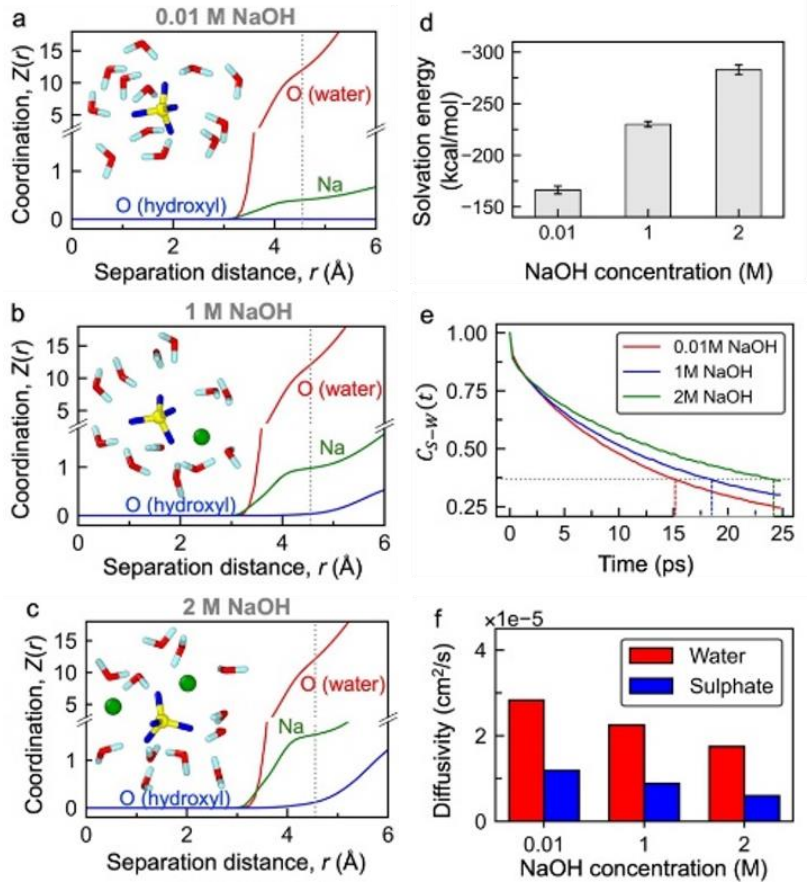

Figure 4. Classical molecular dynamics simulations reveal the role of electrolytes' alkalinity on sulfate transport. (a-c) *Z(r)* of Na^+ (green), O (from OH^-, blue), and O (from water, red) around sulfate in 0.2 M Na_2SO_4 at different NaOH concentrations. The dotted line denotes the first solvation shell at 4.55 Å. The atomic configuration of the solvation shells around SO_4^{2-} is shown as an inset, where Na, S, O, and H atoms are in green, yellow, red, and aqua, respectively. (d) The average interaction energy between sulfate, water, and NaOH molecules in the first solvation shell. (e) Temporal evolution of bond-correlation function $C_{S\text{-}W}(t)$ tracks the association dynamics between sulfate-water pairs within a solvation shell. The grey dotted line refers to $C_{S\text{-}W} = 1/e$. The red, blue, and green dotted lines indicate the lifetime of sulfate-water association in the solvation shells. (f) Diffusivity of water (red) and sulfate anions (blue) at different NaOH concentrations.

Our DFT calculations examined $Fe(OH)_2$ oxidation with a water molecule, hydroxyl, and sulfate ions (**Figure S19**). We assumed H extraction from $Fe(OH)_2$ to be a critical step during oxidization to FeOOH and accordingly modeled this step. H removal from the Fe-O framework is

highly endothermic (2.85 eV) in the presence of water, suggesting $Fe(OH)_2$ oxidation in the neutral electrolyte is sluggish. H removal is the least endothermic (0.62 eV) with hydroxyl anion present, suggesting high alkalinity favors rapid oxidation of $Fe(OH)_2$ and would form Fe_3O_4 experimentally (**Figure 2**). In contrast, $Fe(OH)_2$ oxidation with sulfate ions (1.67 eV) suggested a modest H removal process by theory and demonstrated FeOOH formation experimentally.

In conclusion, we have demonstrated stable $Fe(OH)_2$/FeOOH redox chemistry. We have shown that the intercalation reaction between sulfate and $Fe(OH)_2$ is encouraged in an electrolyte with low alkalinity. The resulting GR phase facilitates the formation of δ-FeOOH. The reported $Fe(OH)_2$/GR/FeOOH redox in a low alkalinity solution applies to other anion systems such as Cl^-, as shown in **Figure S20**. This redox chemistry involving sulfate-insertion processes revitalizes Fe-based anode materials in alkaline batteries for grid-scale storage.

ASSOCIATED CONTENT

Supporting Information

A detailed description of the experimental procedure, CMD calculations, and DFT calculations, **Figures S1-S17**, **Supplementary Table 1.**

AUTHOR INFORMATION

Corresponding Authors

xw.teng@unh.edu;

badri.narayanan@louisville.edu

Notes

The authors declare no competing financial interest.

ACKNOWLEDGMENT

This research received financial support from the US Department of Energy (DOE), Office of Science, Basic Energy Sciences under Awards DE-SC0018922 (FG, SNJ, SK, XS, XT) and DE-SC0021257 (RP, BN). This research used 28-ID-1 beamlines of the National Synchrotron Light Source II, a US Department of Energy (DOE) Office of Science User Facility operated for the

DOE Office of Science by Brookhaven National Laboratory under Contract No. DE-SC0012704. This research used resources of the National Energy Research Scientific Computing Center, a DOE Office of Science User Facility supported by the Office of Science of the U.S. Department of Energy under Contract No. DE-AC02-05CH11231 (RP, BN).

REFERENCES

(1) Dunn, B.; Kamath, H.; Tarascon, J. M. Electrical Energy Storage for the Grid: A Battery of Choices. *Science (80-.).* **2011**, *334* (6058), 928–935.

(2) Xing, Z.; Wang, S.; Yu, A.; Chen, Z. Aqueous Intercalation-Type Electrode Materials for Grid-Level Energy Storage: Beyond the Limits of Lithium and Sodium. *Nano Energy*. Elsevier August 1, 2018, pp 229–244.

(3) Wu, X.; Markir, A.; Xu, Y.; Zhang, C.; Leonard, D. P.; Shin, W.; Ji, X. A Rechargeable Battery with an Iron Metal Anode. *Adv. Funct. Mater.* **2019**, *29* (20), 1900911.

(4) Chakkaravarthy, C.; Periasamy, P.; Jegannathan, S.; Vasu, K. I. The Nickel/Iron Battery. *J. Power Sources* **1991**, *35* (1), 21–35.

(5) Shukla, A. K.; Ravikumar, M. K.; Balasubramanian, T. S. Nickel/Iron Batteries. *J. Power Sources* **1994**, *51* (1–2), 29–36.

(6) Wang, H.; Liang, Y.; Gong, M.; Li, Y.; Chang, W.; Mefford, T.; Zhou, J.; Wang, J.; Regier, T.; Wei, F.; Dai, H. An Ultrafast Nickel-Iron Battery from Strongly Coupled Inorganic Nanoparticle/Nanocarbon Hybrid Materials. *Nat. Commun.* **2012**, *3*, 917.

(7) Manohar, A. K.; Yang, C.; Narayanan, S. R. The Role of Sulfide Additives in Achieving Long Cycle Life Rechargeable Iron Electrodes in Alkaline Batteries. *J. Electrochem. Soc.* **2015**, *162* (9), A1864–A1872.

(8) Mitra, D.; Rajan, A. S.; Irshad, A.; Narayanan, S. R. High Performance Iron Electrodes with Metal Sulfide Additives. *J. Electrochem. Soc.* **2021**, *168* (3), 030518.

(9) Pourbaix, M. *Atlas of Electrochemical Equilibria in Aqueous Solutions*, 2nd ed.; National Association of Corrosion Engineers: Houston - Tex, 1974.

(10) Manohar, A. K.; Malkhandi, S.; Yang, B.; Yang, C.; Surya Prakash, G. K.; Narayanan, S. R. A High-Performance Rechargeable Iron Electrode for Large-Scale Battery-Based Energy Storage. *J. Electrochem. Soc.* **2012**, *159* (8), A1209–A1214.

(11) Malkhandi, S.; Yang, B.; Manohar, A. K.; Prakash, G. K. S.; Narayanan, S. R. Self-Assembled Monolayers of n-Alkanethiols Suppress Hydrogen Evolution and Increase the Efficiency of Rechargeable Iron Battery Electrodes. **2012**, *J. Am. Chem. Soc.* **2013**, *135*, 1, 347–353.

(12) Falk , Salkind, Alvin J., S. U. *Alkaline Storage Batteries*; John Wiley & Sons: New York, 1969.

(13) Majzlan, J.; Lang, B. E.; Stevens, R.; Navrotsky, A.; Woodfield, B. F.; Boerio-Goates, J. Thermodynamics of Fe Oxides: Part I. Entropy at Standard Temperature and Pressure and Heat Capacity of Goethite (α-FeOOH), Lepidocrocite (γ-FeOOH), and Maghemite (γ-Fe_2O_3). *Am. Mineral.* **2003**, *88* (5–6), 846–854.

(14) Toby, B. H.; Von Dreele, R. B. GSAS-II: The Genesis of a Modern Open-Source All Purpose Crystallography Software Package. *J. Appl. Crystallogr.* **2013**, *46* (2), 544–549.

(15) Momma, K.; Izumi, F. VESTA 3 for Three-Dimensional Visualization of Crystal, Volumetric and Morphology Data. *J. Appl. Crystallogr.* **2011**, *44* (6), 1272–1276.

(16) Wyckoff, R. W. G. *Crystal Structures - Volume 1.*; Interscience Publishers: New York, 1963.

(17) Usman, M.; Byrne, J. M.; Chaudhary, A.; Orsetti, S.; Hanna, K.; Ruby, C.; Kappler, A.; Haderlein, S. B. Magnetite and Green Rust: Synthesis, Properties, and Environmental Applications of Mixed-Valent Iron Minerals. *Chem. Rev.* **2018**, *118* (7), 3251–3304.

(18) Génin, J.-M. R.; Bourrié, G.; Trolard, F.; Abdelmoula, M.; Jaffrezic, A.; Refait, P.; Maitre, V.; Humbert, B.; Herbillon, A. Thermodynamic Equilibria in Aqueous Suspensions of Synthetic and Natural Fe(II)−Fe(III) Green Rusts: Occurrences of the Mineral in Hydromorphic Soils. *Environ. Sci. Technol.* **1998**, *32* (8), 1058–1068.

(19) Simon, L.; François, M.; Refait, P.; Renaudin, G.; Lelaurain, M.; Génin, J. M. R. Structure of the Fe(II-III) Layered Double Hydroxysulphate Green Rust Two from Rietveld Analysis. *Solid State Sci.* **2003**, *5* (2), 327–334.

(20) Patrat, G.; de Bergevin, F.; Pernet, M.; Joubert, J. C. Structure Locale de δ-FeOOH. *Acta Crystallogr. Sect. B* **1983**, *39* (2), 165–170.

(21) Wei, L.; Wu, M. C.; Zhao, T. S.; Zeng, Y. K.; Ren, Y. X. An Aqueous Alkaline Battery Consisting of Inexpensive All-Iron Redox Chemistries for Large-Scale Energy Storage. *Appl. Energy* **2018**, *215*, 98–105.

(22) Liu, J.; Chen, M.; Zhang, L.; Jiang, J.; Yan, J.; Huang, Y.; Lin, J.; Fan, H. J.; Shen, Z. X. A Flexible Alkaline Rechargeable Ni/Fe Battery Based on Graphene Foam/Carbon Nanotubes Hybrid Film. *Nano Lett.* **2014**, *14* (12), 7180–7187.

(23) Owusu, K. A.; Qu, L.; Li, J.; Wang, Z.; Zhao, K.; Yang, C.; Hercule, K. M.; Lin, C.; Shi, C.; Wei, Q.; Zhou, L.; Mai, L. Low-Crystalline Iron Oxide Hydroxide Nanoparticle Anode for High-Performance Supercapacitors. *Nat. Commun.* **2017**, *8* (1), 14264.

(24) Ma, Y.-M.; Zhang, H.; Zhang, B.-J. Structure of Sodium Sulphate Aqueous Solution/Quartz Interface: A Molecular Dynamics Simulation. *Mol. Simul.* **2014**, *40* (7–9), 634–639.

(25) Gao, B.; Liu, Z. A First Principles Study on the Solvation and Structure of $SO_4^{2-}(H_2O)_n$, n=6–12. *J. Chem. Phys.* **2004**, *121* (17), 8299–8306.

(26) Pegado, L.; Marsalek, O.; Jungwirth, P.; Wernersson, E. Solvation and Ion-Pairing Properties of the Aqueous Sulfate Anion: Explicit versus Effective Electronic Polarization. *Phys. Chem. Chem. Phys.* **2012**, *14* (29), 10248–10257.

(27) Starr, F. W.; Nielsen, J. K.; Stanley, H. E. Fast and Slow Dynamics of Hydrogen Bonds in Liquid Water. *Phys. Rev. Lett.* **1999**, *82* (11), 2294–2297.

(28) Narayanan, B.; Deshmukh, S. A.; Sankaranarayanan, S. K. R. S.; Ramanathan, S. Strong Correlations between Structural Order and Passive State at Water–Copper Oxide Interfaces. *Electrochim. Acta* **2015**, *179*, 386–393.